International Journal of Heat and Technology
Vol. 43, No. 2, April, 2025, pp. 721-730
Journal homepage: http://iieta.org/journals/ijht

Assessing the Impact of Cavity Structure on Collector and Using PCMs on Solar Chimney Power Plant Performance

Manar Mohammed[1,2*], Moharram Jafari[1], Faramarz Ranjbar[1], Leili Garousi Farshi[1]

[1] Department of Mechanical Engineering, University of Tabriz, Tabriz 5166614766, Iran
[2] Department of Mechanical Power Techniques Engineering, Technical College Engineering Kirkuk, Northern Technical University, Kirkuk 36001, Iraq

Corresponding Author Email: manarmohammed@ntu.edu.iq

https://doi.org/10.18280/ijht.430231

Received: 3 February 2025
Revised: 24 March 2025
Accepted: 8 April 2025
Available online: 30 April 2025

Keywords:
solar energy, SCPP, cavity, PCM, Liquid fraction

ABSTRACT

In the present study, the impact of the type of phase change material (PCM) and the type of cavities created on the collector of a solar chimney power plant (SCPP) on power output has been investigated, numerically. The structure of the cavities applied is a rectangular shape and triangular shape, which have the same and constant size. Also, two types of PCMs, paraffin wax, and SAT-G, have been used. To evaluate the performance of the SCPP, studies for thermal radiation of 700, 1000, and 1300 W/m^2 have been conducted. The results reveal that with increasing heat flux, the output power increases. Also, the results obtained show that rectangular cavities create a stronger velocity field than triangular ones at the chimney base. In this regard, the solar power plant with rectangular cavities produces 30%, 32%, and 21% more power than the triangular case at heat fluxes of 700, 1000, and 1300 W/m^2, respectively. In addition, the use of PCMs leads to the melting and storage of solar energy during the day. An examination of the melting process of PCMs indicates that the PCM of an SAT-G melts later than paraffin wax. In other words, SAT-G as a PCM stores more energy than paraffin wax.

1. INTRODUCTION

Solar energy is a renewable resource that many countries use to manage electricity consumption and develop infrastructure. Solar power plants convert solar energy into electricity, and among these, SCPPs are one of the most common and straightforward types, generating electricity by harnessing solar radiation.

An SCPP comprises three key components: a collector, a chimney, and a turbine. By absorbing solar radiation, the collectors create a draft within the chimney, causing high-speed air to strike the turbine blades. This process leads to generating electricity through a generator. In recent years, the rising value of electricity generation has led researchers and industry experts to extensively study SCPPs, as detailed in the following sections.

Toghraie et al. [1] examined how geometric variables—specifically collector radius, collector height, chimney height, and chimney radius—affect the performance of SCPPs. Their findings indicated a positive correlation between collector radius and chimney height, as well as with the overall efficiency and power output of the system. They also identified optimal ranges for both chimney radius and collector height. Guo et al. [2] investigated the performance of a three-dimensional SCPP using the fan model to account for the turbine effect. Their results indicated that the fan model is effective in analyzing the pressure drop in the turbine. Furthermore, they discovered that the angle of the sun's rays significantly influences power output. Nasraoui et al. [3] evaluated the impact of chimney geometry on the power output of a SCPP. They showed that a diverging chimney has better efficiency than a cylindrical one at a constant height. Cottam et al. [4] examined the impact of SCPP dimensions on power generation. They found that the optimal pressure drop is influenced by the radius of the collector and chimney but is not affected by ambient temperature or chimney height. Arzpeymaa et al. [5] studied the impact of chimney configuration on mitigating the negative effects of wind speed on SCPPs numerically. They demonstrated that the exit angle of the chimney opening is dependent on wind direction for optimal performance of the solar power plant. Cao et al. [6] introduced a novel approach to reduce the height of a solar chimney by using two nested chimneys instead of a single tall one. Their results showed a power output that was 2.77 times greater than that of the conventional design. Fallaah and Valipoour [7] studied the three-dimensional velocity and temperature distribution in a conventional SCPP. The results indicated that a reduction in chimney height leads to a decrease in flow velocity, while the temperature at the chimney inlet increases slightly by approximately 1%. Belkhode et al. [8] tested the optimal design of the chimney geometry by evaluating experimental results. They found that in the proposed geometry, the power plant's performance improves with increasing chimney height. Wang et al. [9] assessed the impact of using baffles with different geometries under the collector on the pressure distribution field, velocity, and power

generation. They demonstrated that employing baffles enhances the velocity and pressure fields in comparison to the conventional setup. Abdelsaalam et al. [10] presented an innovative concept to improve the efficiency of SCPPs. They proposed a dual chimney system, where the inner chimney operates as a traditional chimney, while the outer chimney integrates a cooling tower. Their findings indicated that the proposed SCPP produced 2.6 times more power than a conventional system. Mirzamohammad et al. [11] evaluated the power generation of a SCPP integrated with a gas power plant. The hot exhaust gas from the gas power plant was passed through a pipe buried underground beneath the solar collector. Results showed that at a heat flux of 200 W/m², the proposed power plant generated 554% more power than the conventional setup. Kumar Mandal et al. [12] tested the impact of divergent chimney and inclined absorber on the power output of a SCPP numerically. The findings revealed that the use of divergent chimney and inclined absorber leads to an 80% increase in power generation than the conventional case. Shabahang Nia and Ghazikhani [13] conducted both numerical and experimental investigations on the dimensions of a small SCPP. Their findings showed that increasing the collector radius, chimney height, and chimney radius leads to an increase in power output. Conversely, increasing the collector height negatively impacts the performance of the power plant. Setayesh et al. [14] conducted a numerical evaluation of the SCPP's performance, focusing on its geometric dimensions in an unsteady state. Their results indicated that air flow velocity significantly impacts power generation in the plant. They also discovered that increasing the collector radius leads to a 56% rise in flow velocity. Furthermore, while the radius of the chimney has a minor effect on SCPP performance, its height has a more substantial influence.

One of the most significant challenges of SCPPs is the cessation of electricity generation in the absence of sunlight. In other words, these power plants cannot produce electricity at night. To address this issue, many researchers have explored methods for storing the energy generated during the day so that it can be utilized at night. For example, Méndez and Bicer [15] introduced an energy storage system for a SCPP. In their study, they utilized four types of PCM located in the chimney section. The results indicated that using magnesium chloride hexahydrate as the PCM resulted in the highest heat storage compared to other materials and increased the power generation of the plant throughout the year. Arefian et al. [16] examined the performance of a SCPP equipped with a thermal energy storage system. They employed water bags and packages of moist soil. The findings revealed that using moist soil for thermal energy storage was more effective than using water bags. Ikhlef et al. [17] tested a SCPP that included a thermal storage system experimentally. In order to store heat, they placed the ground beneath the collector with crushed sand. They showed that the crushed sand increased the collector efficiency to 89.73%. Shabahang Nia and Ghazikhani [18] studied how the use of PCMs affects the exergy and efficiency of a SCPP. Their findings indicated that incorporating PCMs enhances the flow rate both during the day and at night, as well as improves exergy. Fadaei et al. [19] conducted an experimental study on the impact of latent heat energy storage on the performance of a SCPP. They used paraffin wax as the PCM within the collector. The findings revealed that incorporating PCMs resulted in a 33.8% increase in flow rate.

The use of PCMs for thermal energy storage in SCPPs is rarely found in the literature. Nevertheless, PCMs have significant potential for efficiently storing heat at low temperatures. In the absence of sunlight, especially during nighttime hours, they can release latent heat to increase the temperature of the working fluid [20]. In many research studies, PCM have been used as a tool for storing solar energy, examples of which are presented below:

Huang et al. [21] conducted experimental investigations on how PCMs affect the performance of solar chimneys. Their results showed that, without sunlight, the chimney could maintain adequate ventilation for up to 10 hours by releasing the latent heat stored in the PCMs. Saravanan et al. [22] evaluated a solar water heater containing PCMs for heat storage numerically. They showed that the system with PCMs stored 320% more energy than the system without them. Hatamleh et al. [23] studied the impact of PCMs on the performance of solar air heaters. Their findings indicated that incorporating PCMs results in reduced energy consumption throughout the year. Tiji et al. [24] employed a solar chimney for room heating, incorporating a fin and a PCM. They demonstrated that the PCM helps maintain the chimney's functionality even when the sun is not shining. Furthermore, the addition of the fin enhances the temperature increase.

By reviewing past studies, it is evident that most research related to SCPPs focuses on optimizing the size of the power plant, with very few new ideas presented. In this study, a novel solar power plant structure is proposed that utilizes cavity-like fins on the collector and PCMs to enhance solar energy absorption, heat transfer, and energy storage during non-solar hours. The introduction of rectangular and triangular cavities to increase output power is presented for the first time in this study. This approach is more innovative compared to previous studies that primarily concentrate on optimizing the geometry of the power plant. This research aims to increase power generation efficiency through the careful selection of PCMs and cavity geometry.

2. PHYSICAL STATEMENT OF THE PROBLEM AND NUMERICAL DETAILS

In this research, a SCPP with an innovative structure has been studied. This power plant consists of a collector to absorb solar radiation, a tall chimney, rectangular and triangular cavities on the collector, and PCMs. The geometry includes several physical characteristics: chimney height (H) is 3 meters, chimney radius (r) is 0.1 meters, collector radius (R) is 3.5 meters, and the height of the collector from the ground (h) is 0.06 meters, as reported by Yapıcı et al. [25]. Figure 1 and Table 1 illustrate the schematic and geometric specifications of the SCPP under investigation. As depicted in Figure 1, fin-like cavities have been created on the collector, and PCMs have been embedded around these fins.

Table 1. Introducing geometric parameters with dimensions

Geometric Parameters	Value
Chimney radius (r)	10 cm
Chimney height (H/r)	30
Collector height from ground level (h/r)	0.6
Collector radius (R/r)	15
Distance between two cavities (B/r)	3.5
PCM thickness (b/r), (b_T/r)	0.4, 0.8
Fin thickness (t/r), (t_T/r)	0.1, 0.2
Cavity height (h_f/r)	0.3
Inlet length (L_i/r), (L_{Ti}/r)	1.9

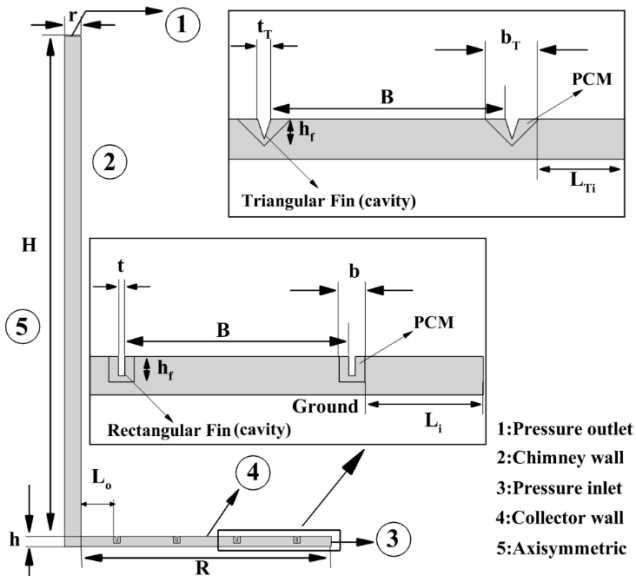

Figure 1. Geometry and details of the studied SCPP with rectangular and triangular cavities with applied boundary conditions

All parameters in Table 1 are normalized with respect to the chimney radius. The dimensions of the cavities and PCMs are selected to ensure equal cross-sectional areas in both rectangular and triangular configurations. Furthermore, the cavity spacing (B) and height (h_f) are kept constant for both geometries. Two types of PCMs with varying thermal properties are employed in this study to examine their influence on daytime thermal energy storage for nighttime utilization. The thermal properties of these materials are listed in Table 2.

Table 2. Thermal properties of PCMs used in this research

Properties	Paraffin Wax R56-58 [26]	SAT-G [27]
Melting temperature (K)	339.65	339.65
Solidification temperature (K)	323.75	323.31
Specific heat (kj/kg.k)	2.1	3.68
Density (kg/m^3)	840	819
Conductivity coefficient (W/m.k)	0.2	5
Latent heat (kj/kg)	120.7	173

In this study, to evaluate the thermal performance and power generation of the SCPP, the effect of parameters such as the type of cavity shape (rectangular and triangular) and the type of PCM has been investigated numerically. Simulations have been carried out for one scenario: the presence of the sun with constant radiation (constant flux). It is worth mentioning that constant fluxes of 700, 1000, and 1300 W/m^2 have been studied in this present. Beyond that, the SCPP modeled in 2D due to axial symmetry, and results for rectangular and triangular cavities, and various PCMs, has been compared.

To analyze fluid flow and performance in a SCPP, we have utilized numerical solutions of the continuity, momentum, and energy equations. These equations are presented in tensor form under the assumption of incompressible and free flow [28]:

$$\frac{\partial}{\partial x_i}(u_i) = 0 \tag{1}$$

$$\rho\frac{\partial u_i}{\partial t} + \rho\frac{\partial}{\partial x_j}(u_i u_j) = -\frac{\partial p}{\partial x_i} + \frac{\partial}{\partial x_j}\left[(\mu_t + \mu)\left(\frac{\partial u_i}{\partial x_j} + \frac{\partial u_j}{\partial x_i}\right) - \frac{2}{3}(\mu_i + \mu)\frac{\partial u_i}{\partial x_i}\delta_{ij}\right] + \rho g_i \beta \Delta T \tag{2}$$

$$\rho\frac{\partial T}{\partial t} + \rho\frac{\partial}{\partial x_j}(u_i T) = \frac{\partial}{\partial x_j}\left[\left(\frac{\mu}{Pr} + \frac{\mu_t}{\sigma_t}\right)\frac{\partial T}{\partial x_j}\right] \tag{3}$$

In the aforementioned equations, Pr and σ_t represent the Prandtl number and turbulent Prandtl number, respectively. Additionally, the parameters μ and μ_t signify viscosity and turbulent viscosity. In Eq. (2), the last term on the right-hand side represents the buoyancy force, and the symbol δ denotes the Kronecker delta. An important point in the continuation of modeling is to identify the flow regime, for which the Rayleigh number (Ra) is used [29]:

$$\mathrm{Ra} = \frac{g\beta/\Delta T L^3}{\alpha \upsilon^2} = \mathrm{Gr} \times \mathrm{Pr} \tag{4}$$

where, L represents the characteristic length, β denotes the coefficient of thermal expansion, α indicates the thermal diffusivity, and υ denotes the kinematic viscosity. Additionally, Gr signifies the Grashof number. Given the dimensions of the geometry investigated, Ra exceeds 10^5, leading to turbulent flow. Consequently, the RNG k-ε turbulence model is employed to model this flow. It is important to note that the efficiency and validity of this model for simulating SCPPs have been validated in numerous studies, including [29-32]. The momentum equation is rewritten as Eqs. (5) and (6) using the turbulence model [32]:

$$\rho\frac{\partial(k)}{\partial t} + \rho\frac{\partial}{\partial x_i}(k u_i) = \frac{\partial}{\partial x_j}\left[\alpha_k \mu_{eff}\frac{\partial k}{\partial x_j}\right] + G_k + G_b + \rho\varepsilon - Y_M + S_k \tag{5}$$

$$\rho\frac{\partial(\varepsilon)}{\partial t} + \rho\frac{\partial}{\partial x_i}(\varepsilon u_i) = \frac{\partial}{\partial x_j}\left[\alpha_\varepsilon \mu_{eff}\frac{\partial \varepsilon}{\partial x_j}\right] + C_{1\varepsilon}\frac{\varepsilon}{k}(G_k + C_{3\varepsilon}G_b) - C_{2\varepsilon}\rho\frac{\varepsilon^2}{k} - R_\varepsilon + S_\varepsilon \tag{6}$$

The presence of a velocity gradient in the flow generates turbulent kinetic energy, denoted as G_k in Eqs. (5) and (6). Additionally, G_b represents the production of turbulent kinetic energy caused by the buoyancy force, expressed as follows:

$$G_k = -\rho u_i u_j \frac{\partial u_i}{\partial u_j} \tag{7}$$

$$G_b = \beta g_i \frac{\mu_t}{Pr_t}\frac{\partial t}{\partial x_i} \tag{8}$$

α_k and α_e denote the inverse effective Prandtl numbers for k and $\boldsymbol{e}$, respectively, while S_k and S_e represent the source terms. In Eq. (5), the term Y_M reflects the influence of incompressible flow fluctuations on the total energy dissipation rate, which is

defined as:

$$Y_M = 2\rho\varepsilon M_t^2 \quad (9)$$

M_t illustrates the Mach number and R_e is the additional term that distinguishes the k-$\boldsymbol{e}$ RNG turbulence model from the standard case and is obtained as follows:

$$R_\varepsilon = \frac{C_\mu \rho \eta^3 (1-\eta/\eta_b)}{1+\beta\eta^3} \frac{\varepsilon^2}{k} \quad (10)$$

It should be noted that the parameters used in the above equation are explained in detail in study [33].

One of the most important performance parameters investigated in this research is the power output of the SCPP produced by the turbine, which is calculated as follows [29]:

$$P_{act} = \eta_t \times \Delta P \times Q \quad (11)$$

In this context, $\boldsymbol{h}_t$ refers to the turbine efficiency, which is set at 0.8 according to Keshari et al. [30]. The term ΔP indicates the pressure drop, calculated as the product of the average pressure at the chimney base and the pressure drop rate, with the pressure drop rate valued at 2/3 [34]. Additionally, Q represents the volume flow rate through the chimney base.

The governing equations are solved numerically using computational fluid dynamics based on the finite volume method. The advection and viscous terms are discretized with second-order upwind schemes, while temporal discretization employs a second-order implicit formulation. The velocity-pressure coupling is resolved using the SIMPLE algorithm, and pressure interpolation is handled via the PRESTO scheme [33].

3. EXAMINING THE SENSITIVITY OF RESULTS TO GRID SIZE

Mesh generation is one of the most critical parameters affecting the results of numerical simulations. Particularly, choosing the appropriate number of mesh elements can significantly reduce computational time and cost while ensuring the reliability of the obtained results. In this study, to enhance computational accuracy, grid size study has been investigated separately for both rectangular and triangular cavities. Figures 2 and 3 demonstrate the applied mesh distribution for rectangular and triangular cavities, respectively. As shown, the computational domain for both cases is divided into three regions: the phase change material, the region beneath the collector, and the solar chimney section. An unstructured mesh is employed for the beneath the collector region and PCM due to the presence of cavities, while a structured mesh is used for the solar chimney domain. Table 3 presents the number of grid cells for the SCPP with both rectangular and triangular fins. It's important to highlight that the dimensions used for both triangular and rectangular cases are identical.

To evaluate the sensitivity of the results to grid size, variations in the liquid fraction of the PCM are presented in Figure 4 for both rectangular and triangular cases. This sensitivity is tested under a constant heat flux of 760 W/m² using paraffin wax as the PCM. As shown in Figure 4, grids of types 1 and 2 deviate significantly from grids 3 and 4, while grids 3 and 4 are in good agreement with each other. In other words, as the number of grid elements increases, the deviation of the result curves from one another for changes in liquid fraction decreases. This observation holds true for both rectangular and triangular cases. To reduce computational time and cost, we have selected grid 3, which contains 101,157 cells in rectangular mode and 100,931 cells in triangular mode.

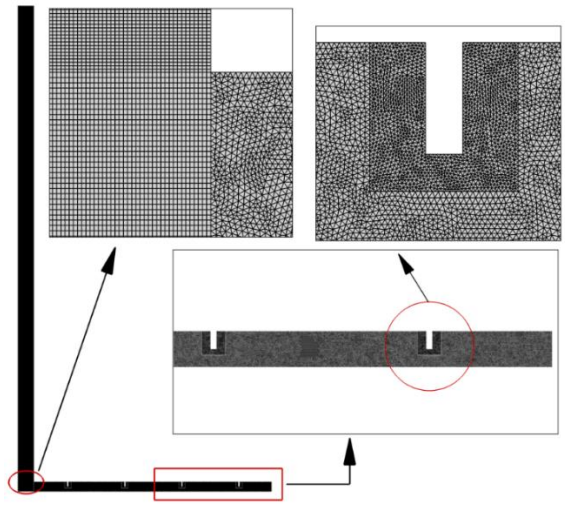

Figure 2. Distribution of applied grids in computational domains for rectangular cavities

Table 3. Number of grids applied for rectangular and triangular modes

	Cell Number	
Grid No.	**Rectangular Cavity**	**Triangular Cavity**
1	17,530	18,480
2	55,145	54,095
3	101,157	100,931
4	157,443	156,326

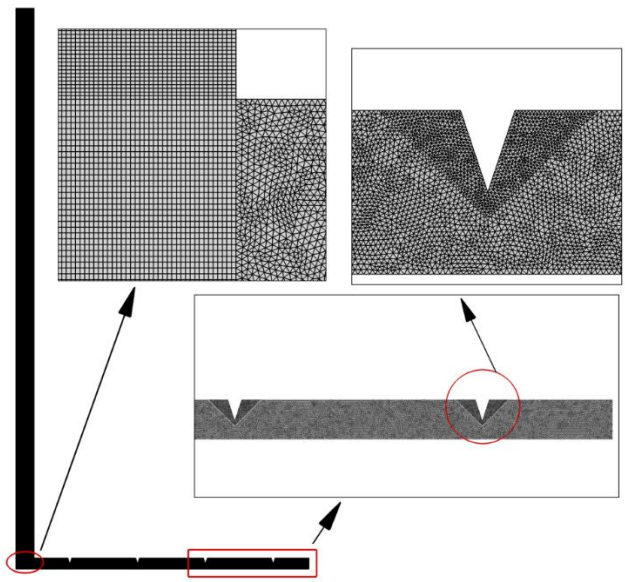

Figure 3. Distribution of applied grids in computational domains for triangular cavities

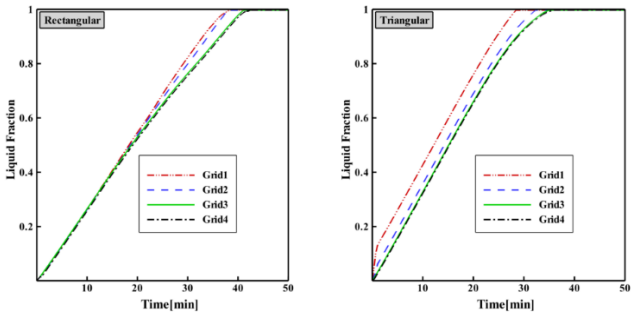

Figure 4. Paraffin wax liquid fraction variation over time for different grid arrangements for rectangular and triangular cases

4. STUDY OF VALIDATION

The validation of numerical results is essential to confirm the accuracy of the numerical simulation of the SCPP. However, previous studies have not examined a geometry similar to the SCPP that incorporates the desired PCMs. To enhance the reliability of the solution model for both the SCPP and the PCMs, we conduct separate validation studies for the power plant and the PCMs. The numerical results of the SCPP are validated against experimental data from Ghalamchi et al. [35] and numerical results from Yapıcı et al. [25].

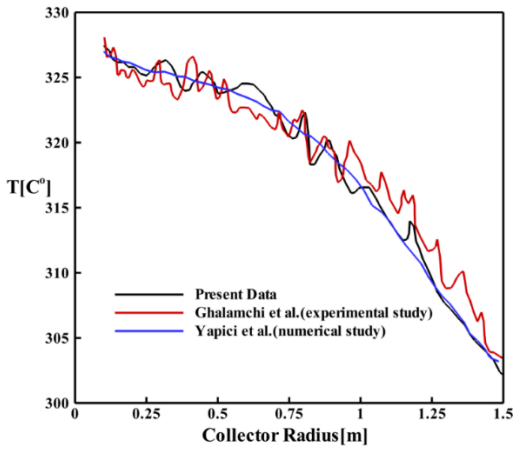

Figure 5. Temperature variations in the collector radius used to validate the SCPP results

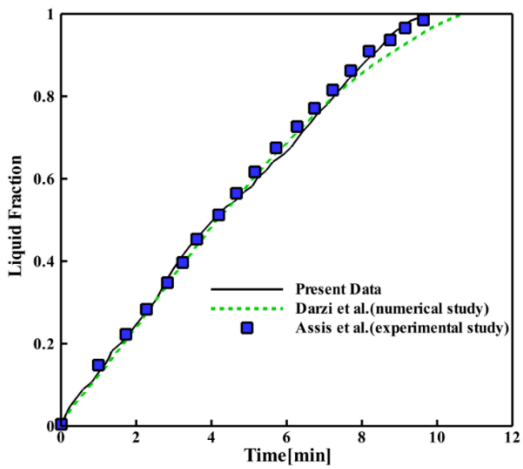

Figure 6. Comparison of changes in liquid fraction in PCMs using numerical and experimental data

Figure 5 compares the temperature distribution along the collector, showing a strong agreement between the current study and previous research. To validate the accuracy of the PCM model, numerical results from Darzi et al. [36] and experimental data from Assis et al. [37] are also utilized. The changes in the liquid fraction of the phase change material, illustrated in Figure 6, closely align with findings reported in the literature.

5. RESULTS AND DISCUSSIONS

5.1 Effect of heat flux

Figure 7 shows the velocity contours at the base of the chimney in the solar power plant, using paraffin wax as the PCM and featuring rectangular cavities, for heat fluxes of 700, 1000, and 1300 W/m². It is clear that as the heat flux increases from 700 to 1300 W/m², the velocity field at the chimney base becomes stronger. Specifically, the weakest velocity field occurs at 700 W/m², while the strongest is observed at 1300 W/m². This indicates that the maximum volumetric flow rate through the chimney base corresponds to a heat flux of 1300 W/m².

Figure 8 presents the pressure contours at the chimney base under the same conditions. The pressure distribution reveals an inverse relationship between the pressure field and heat flux: as the heat flux decreases, the pressure field strengthens. In Figure 8, the pressure field at 1000 W/m² is weaker than at 700 W/m² but stronger than at 1300 W/m². Thus, it can be anticipated that the pressure drop will be greatest at a heat flux of 1300 W/m² compared to the other scenarios.

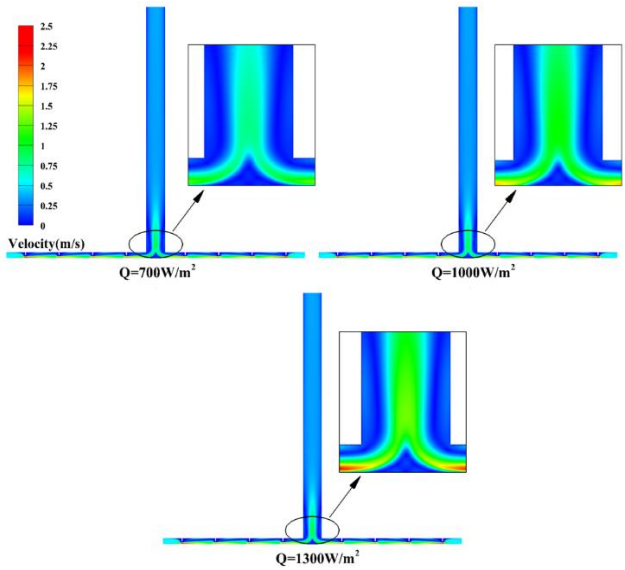

Figure 7. Velocity contours at the base of the chimney in the solar power plant are analyzed for heat fluxes of 700, 1000, and 1300 W/m², utilizing paraffin wax as the PCM within rectangular cavities

Figure 9 shows the variations in pressure, velocity, and temperature profiles at the chimney base concerning the chimney radius for heat flux conditions of 700, 1000, and 1300 W/m², using paraffin wax as the PCM and rectangular cavities. The pressure variation plot indicates that as heat flux increases, pressure decreases. The minimum pressures recorded for heat fluxes of 700, 1000, and 1300 W/m² are -5.5, -6.5, and -7.5 Pa,

respectively. Thus, the lowest pressure occurs at a heat flux of 1300 W/m², which is attributed to a weaker pressure field under these conditions, as illustrated in Figure 8.

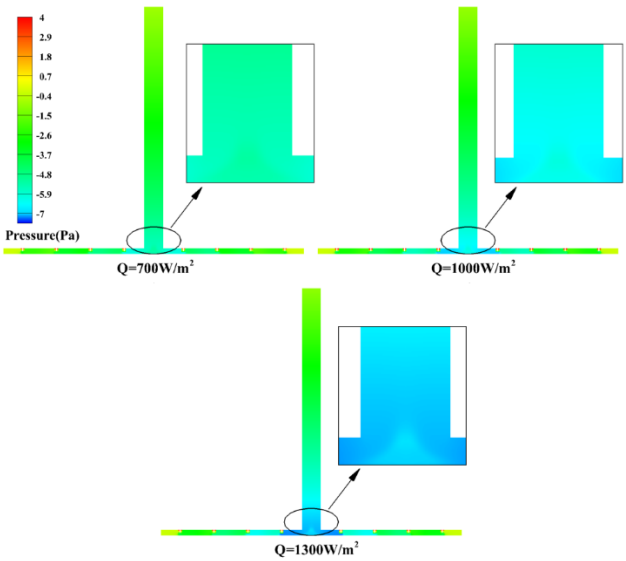

Figure 8. Pressure contours in the solar power plant, specifically at the chimney base, for heat fluxes of 700, 1000, and 1300 W/m², using paraffin wax as the PCM and with rectangular cavities

Examining the velocity profile along the chimney radius reveals that, regardless of heat flux, the velocity decreases from the center to the wall due to the no-slip condition. The velocity reaches its maximum at the center of the chimney, as shown in Figure 7. The results in Figure 9 demonstrate a direct correlation between heat flux and maximum velocity: As heat flux increases, maximum velocity also rises, leading to a higher volumetric flow rate within the chimney. At a heat flux of 1300 W/m², the maximum velocity recorded is 1 m/s.

The final plot in Figure 9 illustrates variations in the temperature profile. Given that the inlet fluid temperature to the solar power plant is 308 K, the temperature profiles indicate a significant increase in fluid temperature within the chimney as heat flux rise.

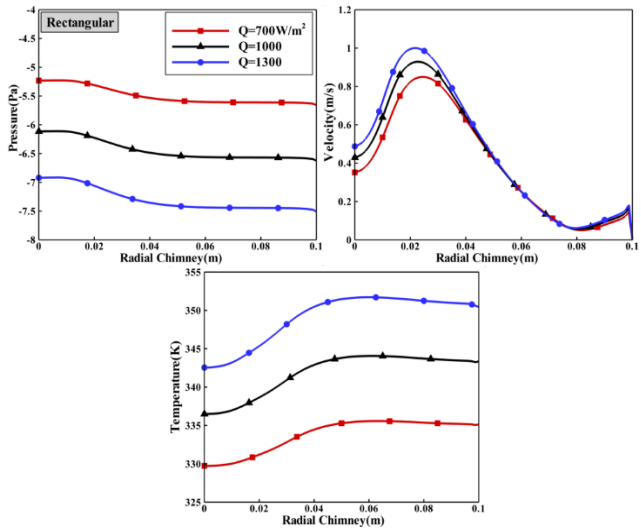

Figure 9. The variations in pressure, velocity, and temperature profiles at the chimney base, relative to the chimney radius, using paraffin wax as the PCM within rectangular cavities

Figure 10 illustrates the change in the liquid fraction of paraffin wax phase change material (PCM) over time within rectangular cavities for heat fluxes of 700, 1000, and 1300 W/m². This diagram clearly demonstrates the melting process of the PCM, showing that higher heat fluxes result in quicker melting and a more rapid increase in the liquid fraction. The complete melting times for the PCM are 45 minutes at 700 W/m², 35 minutes at 1000 W/m², and 20 minutes at 1300 W/m². Thus, as the heat flux increases, the PCM absorbs latent heat at a significantly faster rate.

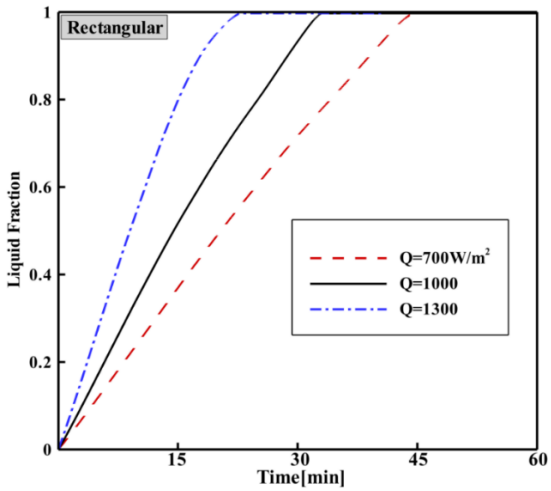

Figure 10. The variation in the liquid fraction of paraffin wax PCM over time in rectangular cavities for heat fluxes of 700, 1000, and 1300 W/m²

5.2 Effect of cavity type and PCM type

Figure 11 displays the velocity (a-b) and pressure (c-d) contours for a SCPP featuring rectangular and triangular cavities under a heat flux of 1000 W/m², using paraffin wax as the PCM. Contours (a) and (b) illustrate the velocity patterns for the rectangular and triangular cavities, respectively. A comparison of these figures reveals that the velocity field is stronger in the rectangular case than in the triangular case at the base of the chimney. Moreover, the flow velocity is higher at the bottom edges of the rectangular cavities compared to the triangular ones. Contours (c) and (d) depict the pressure patterns for the rectangular and triangular cavities, respectively. It is observed that the pressure field at the base of the chimney is weaker and more negative in the rectangular case than in the triangular case, indicating a significant pressure drop in the rectangular cavities.

Figure 12 illustrates the variations in pressure, velocity, and temperature profiles at the chimney base in relation to the chimney radius for rectangular and triangular cavities under a heat flux of 1000 W/m², using paraffin wax as the PCM. A comparison of the pressure variation diagrams reveals that the SCPP with rectangular cavities exhibits the lowest pressure, recorded at -6.6 Pa. In contrast, the pressures at the center of the chimney are -2.6 Pa for rectangular cavities and -5.8 Pa for triangular cavities. This indicates that the pressure drop in rectangular cavities is greater than that in triangular ones, as confirmed by the pressure contours in Figure 11.

Additionally, the velocity profile in Figure 12 shows that the maximum velocity occurs in the rectangular cavity setup, reaching 0.92 m/s, while the triangular setup achieves a maximum of 0.9 m/s. Thus, the results indicate a stronger velocity field at the chimney base for the rectangular

configuration compared to the triangular one, as illustrated by the velocity contours in Figure 11.

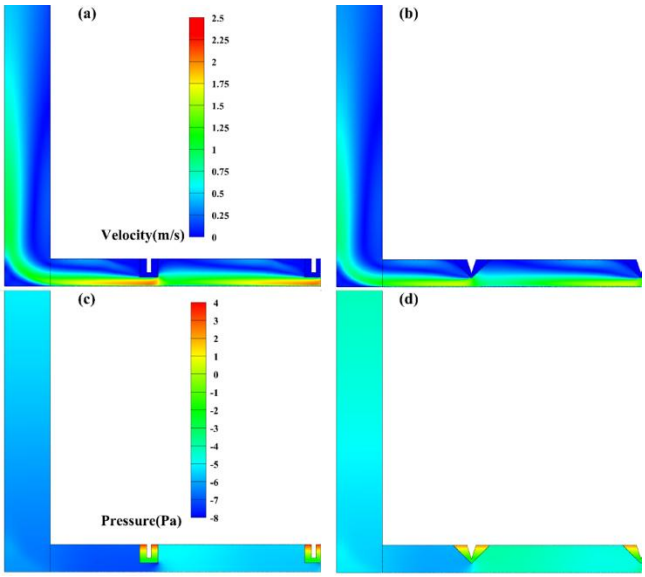

Figure 11. The velocity (a-b) and pressure (c-d) contours for a SCPP with rectangular and triangular cavities, for a heat flux of 1000 W/m² and paraffin wax as the PCM

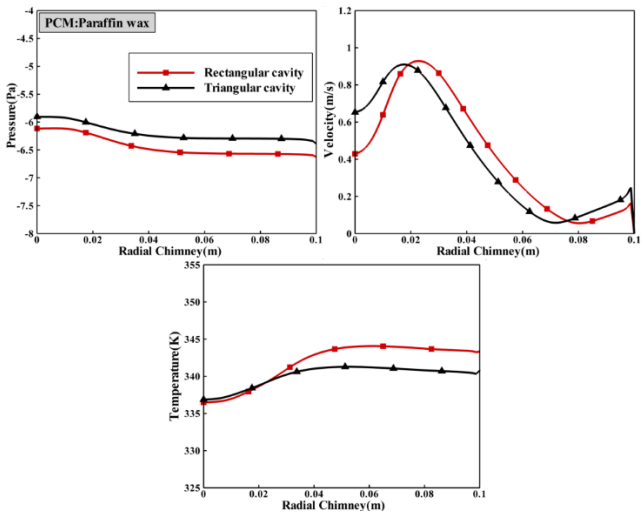

Figure 12. The variations in pressure, velocity, and temperature profiles at the base of the chimney are analyzed under a heat flux of 1000 W/m², using paraffin wax as the PCM

Furthermore, the temperature distribution indicates that the air beneath the collector is hotter in the rectangular cavities than in the triangular ones, resulting in warmer air at the bottom of the chimney with rectangular cavities. Consequently, based on the findings presented in Figure 12, it can be concluded that the power plant utilizing rectangular cavities has the potential to generate more power than the one using triangular cavities.

Figure 13 displays the liquid fraction contour for rectangular and triangular cavities with a heat flux of 1000 W/m² and containing PCMs of paraffin wax and SAT-G for t=15 and 30 min, individually. The liquid fraction contour reveals that the melting amount increased with time, regardless of the cavity type and the type of PCM. Also, the heat penetration for melting the PCM in SAT-G is higher than that of paraffin wax, which can be seen in both rectangular and triangular cases. This phenomenon is due to the higher thermal conductivity of SAT-G PCM compared to paraffin wax. Consequently, paraffin wax PCM tends to melt faster than SAT-G, regardless of the cavity geometry. Figure 13 illustrates that the type of cavity significantly impacts the liquid fraction of PCMs. Notably, triangular cavities exhibit a higher liquid fraction than rectangular cavities for all PCMs. This trend is evident in all contours, particularly at t = 30 min for the same PCM.

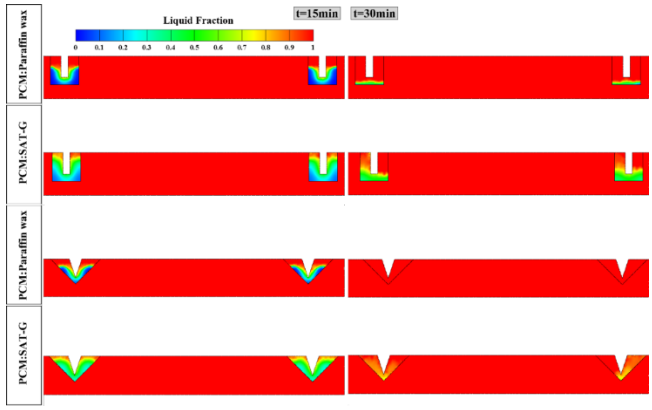

Figure 13. The liquid fraction contour for rectangular and triangular cavities with a heat flux of 1000 W/m² and containing PCMs of paraffin wax and SAT-G for t=15 and 30 min

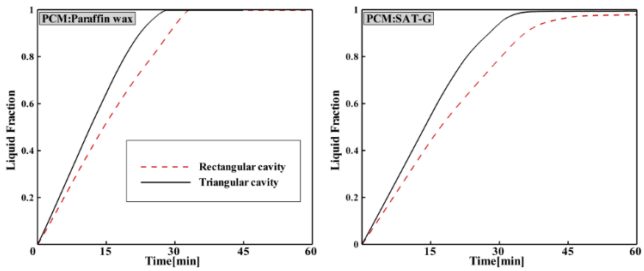

Figure 14. The liquid fraction of paraffin wax and SAT-G PCMs over time for both rectangular and triangular cavity geometries, subjected to a constant heat flux of 1000 W/m²

Figure 14 illustrates the liquid fraction of paraffin wax and SAT-G PCMs over time for both rectangular and triangular cavity geometries, under a constant heat flux of 1000 W/m². The plots show that the melting process for the triangular cavity geometry is completed earlier compared to the rectangular one, regardless of the PCM used. This result can be seen in Figure 15. Moreover, the results indicate that the melting time for paraffin wax in rectangular and triangular cavities is 35 and 28 minutes, respectively, while for SAT-G, these times are 60 and 38 minutes. In other words, triangular cavities transfer heat to the PCM more efficiently than rectangular cavities. Consequently, triangular cavities are more effective in transferring solar energy to the PCM compared to rectangular cavities.

Another observation from Figure 14 is the contrasting thermal performance of paraffin wax and SAT-G PCMs when compared to each other. In this regard, the paraffin wax PCM melted faster than the SAT-G PCM in both rectangular and triangular cavity cases. Figure 13 demonstrates this one. Based on the thermal properties of the PCMs used, it can be inferred that both materials have the same melting point, but different latent heats. The latent heat of SAT-G is higher than that of

paraffin wax. This has caused the SAT-G PCM to require more energy than paraffin wax to melt completely. As a result, the SAT-G PCM stores more energy than paraffin wax.

5.3 Power generation

Power generation is a key parameter for comparing the performance of power plants with rectangular and triangular cavities at various heat fluxes. It is important to note that the numerical power generated by the small-scale SCPP under study is relatively low. However, this section of the article focuses on exploring how cavity shapes affect power generation. Figure 15 displays the power output for different heat fluxes—700, 1000, and 1300 W/m²—for the SCPP equipped with both rectangular and triangular cavities. Since PCMs do not influence power generation, only paraffin wax PCMs were used.

The data in Figure 15 clearly show a direct correlation between increasing heat flux and power output, regardless of cavity configuration. Additionally, the impact of cavity type on power production is evident; the plant with rectangular cavities consistently generated more power than the one with triangular cavities across all heat fluxes. Specifically, the maximum and minimum power outputs were reported for the rectangular and triangular cavities, respectively, at 0.28 watts and 0.14 watts.

A closer examination of Figure 15 reveals that at heat fluxes of 700, 1000, and 1300 W/m², the plant with rectangular cavities produced 30%, 32%, and 21% more power than the triangular configuration, respectively.

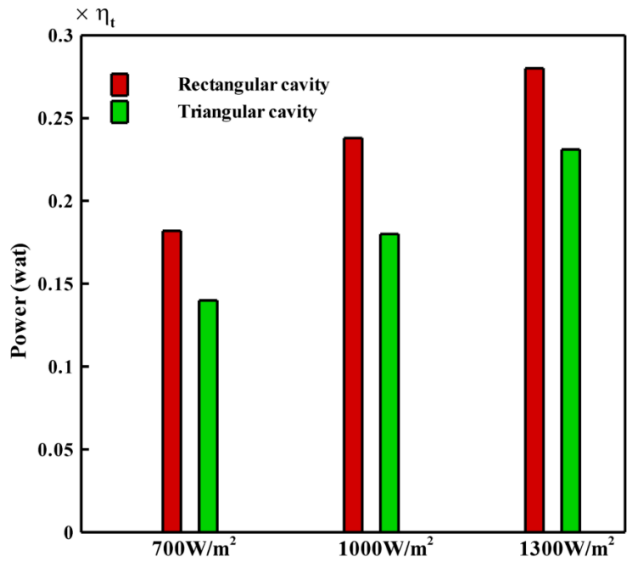

Figure 15. The power output for various heat fluxes, such as 700, 1000, and 1300 W/m², for a SCPP with both rectangular and triangular cavities (PCM: paraffin wax)

6. CONCLUSIONS

In this study, we evaluated the performance of a SCPP that incorporates PCMs and thermal cavities. Notably, the use of thermal cavities represents a novel innovation not previously observed in earlier research. For this purpose, two types of PCMs such as paraffin wax and SAT-G, and two types of cavity structures such as rectangular and triangular were used for examination. All conditions were tested for constant heat fluxes of 700, 1000, and 1300 W/m^2. The findings can be summarized as follows:

• An increase in heat flux intensified the velocity field while weakening the pressure field at the chimney base. Additionally, the maximum velocity rose in proportion to the increase in heat flux. In contrast, the minimum pressure showed an inverse relationship with heat flux. Overall, the power output of the SCPP increased as heat flux rose.

• The type of PCM did not influence power output during heat flux, but the cavity geometry did affect power generation. It was observed that the SCPP with rectangular cavities consistently produced more power than those with triangular cavities at all heat fluxes. The maximum difference in power output between the two cavity types reached 32%.

REFERENCES

[1] Toghraie, D., Karami, A., Afrand, M., Karimipour, A. (2018). Effects of geometric parameters on the performance of solar chimney power plants. Energy, 162: 1052-1061. https://doi.org/10.1016/J.ENERGY.2018.08.086

[2] Guo, P., Li, J., Wang, Y., Wang, Y., Wang, Y. (2015). Numerical study on the performance of a solar chimney power plant. Energy Conversion Management, 105: 197-205. https://doi.org/10.1016/J.ENCONMAN.2015.07.072

[3] Nasraoui, H., Driss, Z., Kchaou, H. (2020). Effect of the chimney design on the thermal characteristics in solar chimney power plant. Journal of Thermal Analysis and Calorimetry, 140: 2721-2732. https://doi.org/10.1007/s10973-019-09037-3

[4] Cottam, P.J., Duffour, P., Lindstrand, P., Fromme, P. (2019). Solar chimney power plants – Dimension matching for optimum performance. Energy Conversion Management, 194: 112-123. https://doi.org/10.1016/J.ENCONMAN.2019.04.074

[5] Arzpeyma, M., Mekhilef, S., Newaz, K.M.S., Horan, B., Seyedmahmoudian, M., Akram, N., Stojcevski, A. (2020). Solar chimney power plant and its correlation with ambient wind effect. Journal of Thermal Analysis and Calorimetry, 141: 649-668. https://doi.org/10.1007/s10973-019-09065-z

[6] Cao, F., Yang, T., Liu, Q., Zhu, T., Li, H., Zhao, L. (2017). Design and simulation of a solar double-chimney power plant. Renewable Energy, 113: 764-773. https://doi.org/10.1016/J.RENENE.2017.05.100

[7] Fallah, S.H., Valipour, M.S. (2022). Numerical investigation of a small scale sloped solar chimney power plant. Renewable Energy, 183: 1-11. https://doi.org/10.1016/J.RENENE.2021.10.081

[8] Belkhode, P., Sakhale, C., Bejalwar, A. (2020). Evaluation of the experimental data to determine the performance of a solar chimney power plant. Materials Today: Proceedings, 27: 102-106. https://doi.org/10.1016/J.MATPR.2019.09.006

[9] Wang, H., Chen, J., Dai, P., Zhang, F., Li, Q. (2021). Simulation and experimental study of the influence of the baffles on solar chimney power plant system. Process, 9(5): 902. https://doi.org/10.3390/PR9050902

[10] Abdelsalam, E., Kafiah, F., Almomani, F., Tawalbeh, M., Kiswani, S., Khasawneh, A., Ibrahim, D., Alkasraw, M. (2021). An innovative design of a solar double-chimney

power plant for electricity generation. Energies, 6235(14): 6235. https://doi.org/10.3390/EN14196235
[11] Mirzamohammad, A., Eftekhari, M., Lavasani, A.M. (2023). Improvment of combined solar chimney power plant with gas power plant. Scientific Reports, 13: 11220. https://doi.org/10.1038/s41598-023-38464-4
[12] Kumar Mandal, D., Biswas, N., Manna, N.K., Benim, A.C. (2024). Impact of chimney divergence and sloped absorber on energy efficacy of a solar chimney power plant (SCPP). Ain Shams Engineering Journal, 15(2): 102390. https://doi.org/10.1016/J.ASEJ.2023.102390
[13] Shabahang Nia, E., Ghazikhani, M. (2023). Dimensional investigation of solar chimney power plant based on numerical and experimental results. Thermal Science and Engineering Progress, 37: 101548. https://doi.org/10.1016/J.TSEP.2022.101548
[14] Setayesh, H., Kasaeian, A., Najafi, M., Pour, M.M., Akbari, M. (2024). The effects of geometric factors on power generation performance in solar chimney power plants. Energy, 310: 133264. https://doi.org/10.1016/J.ENERGY.2024.133264
[15] Méndez, C., Bicer, Y. (2021). Comparison of the influence of solid and phase change materials as a thermal storage medium on the performance of a solar chimney. Energy Science & Engineering, 9(8): 1274-1288. https://doi.org/10.1002/ESE3.892
[16] Arefian, A., Hosseini-Abardeh, R., Rahimi-Larki, M., Torkfar, A., Sarlak, H. (2024). A comprehensive analysis of time-dependent performance of a solar chimney power plant equipped with a thermal energy storage system. Renewable and Sustainable Energy Reviews, 189: 114051. https://doi.org/10.1016/J.RSER.2023.114051
[17] Ikhlef, K., Larbi, S., Üçgül, İ. (2022). Experimental study of different thermal storage system effects on the performance of a small prototype solar chimney power plant. Renewable Energy, 200: 516-526. https://doi.org/10.1016/J.RENENE.2022.09.087
[18] Shabahang Nia, E., Ghazikhani, M. (2024). Enhancing reliability and efficiency of solar chimney by phase change material Integration: An experimental study. Thermal Science and Engineering Progress, 51: 102600. https://doi.org/10.1016/J.TSEP.2024.102600
[19] Fadaei, N., Kasaeian, A., Akbarzadeh, A., Hashemabadi, S.H. (2018). Experimental investigation of solar chimney with phase change material (PCM). Renewable Energy, 123: 26-35. https://doi.org/10.1016/J.RENENE.2018.01.122
[20] Abhat, A. (1983). Low temperature latent heat thermal energy storage: Heat storage materials. Solar Energy, 30(4): 313-332. https://doi.org/10.1016/0038-092X(83)90186-X
[21] Huang, S., Li, W., Lu, J., Li, Y., Wang, Z., Zhu, S. (2024). Experimental study on thermal performances of a solar chimney with and without PCM under different system inclination angles. Energy, 290: 130154. https://doi.org/10.1016/J.ENERGY.2023.130154
[22] Saravanan, M., Arul Selvan, S., Radhakrishnan, N., Rao, S.S., Sharma, V., Madhavarao, S., Siva Chandran, S. (2023). Improving the thermal efficiency of a solar water heater by using PCM. Materials Today: Proceedings, 13: 65-78. https://doi.org/10.1016/J.MATPR.2023.07.233
[23] Hatamleh, R.I., Abu-Hamdeh, N.H., Bantan, R.A.R. (2022). Integration of a solar air heater to a building equipped with PCM to reduce the energy demand. Journal of Building Engineering, 48: 103948. https://doi.org/10.1016/J.JOBE.2021.103948
[24] Tiji, M.E., Eisapour, M., Yousefzadeh, R., Azadian, M., Talebizadehsardari, P. (2020). A numerical study of a PCM-based passive solar chimney with a finned absorber. Journal of Building Engineering, 32: 101516. https://doi.org/10.1016/J.JOBE.2020.101516
[25] Yapıcı, E.Ö., Ayli, E., Nsaif, O. (2020). Numerical investigation on the performance of a small scale solar chimney power plant for different geometrical parameters. Journal of Cleaner Production, 276: 122908. https://doi.org/10.1016/J.JCLEPRO.2020.122908
[26] Buonomo, B., Capasso, L., Diana, A., Manca, O., Nardini, S. (2019). A numerical analysis on a solar chimney with an integrated latent heat thermal energy storage. AIP Conference Proceeding, 2191: 020029. https://doi.org/10.1063/1.5138762/1007433
[27] Talmatsky, E., Kribus, A. (2008). PCM storage for solar DHW: An unfulfilled promise? Solar Energy, 82(10): 861-869. https://doi.org/10.1016/j.solener.2008.04.003
[28] Versteeg, H.K. (2007). An introduction to Computational Fluid Dynamics the Finite Volume Method, 2/E. Pearson Education India.
[29] Mandal, D.K., Biswas, N., Manna, N.K., Benim, A.C. (2024). Impact of chimney divergence and sloped absorber on energy efficacy of a solar chimney power plant (SCPP). Ain Shams Engineering Journal, 15(2): 102390. https://doi.org/10.1016/j.asej.2023.102390
[30] Keshari, S.R., Chandramohan, V.P., Das, P. (2021). A 3D numerical study to evaluate optimum collector inclination angle of Manzanares solar updraft tower power plant. Solar Energy, 226: 455-467. https://doi.org/10.1016/j.solener.2021.08.062
[31] Gholamalizadeh, E., Kim, M.H. (2016). CFD (computational fluid dynamics) analysis of a solar-chimney power plant with inclined collector roof. Energy, 107: 661-667. https://doi.org/10.1016/j.energy.2016.04.077
[32] Cuce, E., Cuce, P.M., Sen, H., Sudhakar, K., Berardi, U., Serencam, U. (2021). Impacts of ground slope on main performance figures of solar chimney power plants: A comprehensive CFD research with experimental validation. International Journal of Photoenergy. https://doi.org/10.1155/2021/6612222
[33] Cuce, E., Sen, H., Cuce, P.M. (2020). Numerical performance modelling of solar chimney power plants: Influence of chimney height for a pilot plant in Manzanares, Spain. Sustainable Energy Technologies and Assessments, 39: 100704. https://doi.org/10.1016/j.seta.2020.100704
[34] Li, J., Guo, H., Huang, S. (2016). Power generation quality analysis and geometric optimization for solar chimney power plants. Solar Energy, 139: 228-237. https://doi.org/10.1016/j.solener.2016.09.033
[35] Ghalamchi, M., Kasaeian, A., Ghalamchi, M., Mirzahosseini, A.H. (2016). An experimental study on the thermal performance of a solar chimney with different dimensional parameters. Renewable Energy, 91: 477-483. https://doi.org/10.1016/j.renene.2016.01.091
[36] Darzi, A.R., Farhadi, M., Sedighi, K. (2012). Numerical study of melting inside concentric and eccentric horizontal annulus. Applied Mathematical Modelling, 36(9): 4080-4086. https://doi.org/10.1016/j.apm.2011.11.033

[37] Assis, E., Katsman, L., Ziskind, G., Letan, R. (2007). Numerical and experimental study of melting in a spherical shell. International Journal of Heat and Mass Transfer, 50(9-10): 1790-1804. https://doi.org/10.1016/j.ijheatmasstransfer.2006.10.007

NOMENCLATURE

B	distance between two cavities, cm
G_b	production of turbulent kinetic energy
G_k	turbulent kinetic energy
Gr	Grashof number
H	chimney height, cm
h	collector height from ground level, cm
h_f	cavity height, cm
M_t	Mach number
P_r	Prandtl number
R	collector radius, cm
r	chimney radius, cm
Ra	Rayleigh number
R_e	additional term
S_k	source terms
S_e	source terms
t	thickness (rectangular)
t_T	thickness (triangular)
Y_M	effect of incompressible flow

Greek symbols

α	thermal diffusivity, m^2. s^{-1}
α_k	inverse effective Prandtl number for k
α_e	inverse effective Prandtl number for e
β	thermal expansion coefficient, K^{-1}
σ	turbulent Pandtl number
δ	Kronecker delta
μ	dynamic viscosity, kg. $m^{-1}.s^{-1}$
μ_t	turbulent viscosity